An Integrated 2-bit all Optical Analog to Digital Converter based on Photonic Crystal Semiconductor Optical Amplifier

Sajjad Moshfe
Science and Research Branch, Islamic Azad University, Tehran
kambiz abedi (k_abedi@sbu.ac.ir)
Faculty of electrical engineering, Shahid Beheshti University
Mohammad Kazem Moravvej-Farshi
Tarbiat Modares University Faculty of Electrical and Computer Engineering https://orcid.org/0000-0002-8954-6418

Research Article

Keywords: Photonic crystal, semiconductor optical amplifier, analog to digital converter

Posted Date: March 12th, 2021

DOI: https://doi.org/10.21203/rs.3.rs-283585/v1

Version of Record: A version of this preprint was published at Optical and Quantum Electronics on April 19th, 2021. See the published version at https://doi.org/10.1007/s11082-021-02858-3.

An integrated 2-bit all optical analog to digital converter based on photonic crystal semiconductor optical amplifier

Sajjad Moshfe[1] Kambiz Abedi[2] Mohammad Kazem Moravvej-Farshi[3ORCID]

Abstract

In this paper, by integrating InP/InGaAsP/InP Photonic crystal semiconductor optical amplifier (PhC-SOA) with photonic crystal channel drop filters (PhC-CDF), we present a novel fully integrated ultra-small low-power all-optical analog to digital converter (AO-ADC). The self-phase modulation in the PhC-SOA can shift the frequency of the Gaussian input pulse. The two output PhC-CDFs are designed in a way that appropriately codes the frequency-shifted pulse by the PhC-SOA, which consequently converts them to four desired digital output levels. The numerical results indicated that the center wavelength of an amplitude modulated Gaussian pulse with a center wavelength of 1551.228 nm, temporal pulse-width of 10.6 ps, and energy of 74.4 fJ can be shifted by 1.652 nm. This shift is accommodated by utilizing a PhC-SOA with a length of 9 μm and an injection current of 6.5 mA. The shifted pulse is then quantized and coded to the four digital levels of (00, 01, 10, 11) by two point-defect PhC-CDFs. The PhC-CDFs minimize the AO-ADC integral and differential nonlinearity (INL/DNL) errors by compensating for the effect of the nonlinear frequency shift induced by PhC-SOA. The proposed design offers a footprint of 142 μm^2 AO-ADC working at 10 Gs/s.

Keywords: Photonic crystal, semiconductor optical amplifier, analog to digital converter

1 Introduction

Regarding the development of the optical network communication systems, similar to other optical gates (Parandin et al. 2021; Parandin, Karkhanehchi 2017; Taleb, Abedi 2013), semi-optical (Taylor et al. 1978; Nathawad et al. 2003), and all-optical analog to digital converters (AO-ADCs) as an inseparable part of any digital system have been proposed in the recent decades.

✉ Mohammad Kazem Moravvej-Farshi
moravvej@modares.ac.ir
Sajjad Moshfe
s.moshfe@srbiau.acir
Kambiz Abedi
k.abedi@sbu.ac.ir

[1] Department of Electrical Engineering, Science and Research Branch, Islamic Azad University, Tehran, 1477893855, Iran

[2] Faculty of Electrical Engineering, Shahid Beheshti University, Tehran, Iran

[3] Nano Plasmo-Photonic Research Group, Faculty of Electrical and Computer Engineering, Tarbiat Modares University, P. O. Box 14115-194, Tehran 1411713116, Iran

ORCID: https://orcid.org/0000-0002-8954-6418

AO-ADCs take advantage of nonlinear properties in optical devices such as fiber, semiconductor optical amplifier (SOA), and Photonic crystals (PhC). Jeong and Marhic (Jeong, Marhic 1992) proposed an AO-ADC based on the Kerr effect by utilizing cross-phase modulation (XPM) in a 200-m single mode fiber loop, working as a nonlinear interferometer. Photonic A/D conversion was to be achieved by using Kerr nonlinearities in hard limiters consisting of alternating layers of nonlinear materials (Brzozowski, Sargent 2001). Other studies proposed the use of mechanisms such as self-frequency shifting (Xu, Liu 2003; Nishitani et al. 2005) and slicing the supercontinuum spectrum (Oda, Maruta 2005), in long fibers. Filtering a broadened and split spectrum induced by Soliton effects and self-phase modulation (SPM) in optical fiber was another technique used to develop an AO-ADC (Oda, Maruta 2006). To improve the bit resolution in photonic A/D conversion identical half-wave voltages in Mach-Zehnder modulators (Yang et al. 2009), self-frequency shifting, and SPM induced spectral compression were used (Nishitani et al. 2008). In 2011, a five-bit AO-ADC for operation at 40 Gb/s was also developed (Konishi et al. 2011). By replacing the high-nonlinear fiber with a shorter photonic crystal fiber, a 6-bit AO-ADC was achieved (Zhe et al. 2013). Recently, the development of an AO-ADC based on the intensity-to-wavelength conversion by soliton self-frequency shift, operating at 40 Gs/s, has been reported (Nagashima et al. 2017). Nonetheless, fiber-based AO-ADCs are not suitable for integration.

Meanwhile, using nonlinearities in SOAs and PhC channel drop filters (PhC-CDFs) (Youssefi et al. 2012; Mehdizadeh et al. 2017c, b, a; Jafari et al. 2018; Baghbanzadeh, Andalib 2020; Khosroabadi et al. 2020; Sani et al. 2020b; Shamsi, Moradi 2020; Xin, Linfeng 2020), researchers published various design of integrated AO-ADCs. The integrable AO-ADC based on SOA was first reported in (Scaffardi et al. 2009), where the cross-gain modulation (XGM) of SOA was used to quantize analog signal into 4 level digital outputs at 20 Gs/s. However, as the number of the quantization levels (QL) is increased, this design faces the complexity of the AO-ADC structure, requiring (2QL+1) SOAs, and the quantization levels become hardly distinct. In an alternative design, (Wen et al. 2012) exploited polarization switches based on the nonlinear polarization rotation in SOA to achieve a 3-bit AO-ADC operating at hundreds of Gs/s. Using multiple rectangular bandpass filters to digitize the chirped probe signal passing through a quantum dot SOA (QDSOA), Hoshino et. al. revealed a 3-bit AO-ADC based on QDSOA, operating at 10 Gs/s with an 8-level optical quantization (Hoshino et al. 2018). (Moshfe et al. 2020) proposed a 2-bit AO-ADC using the SPM effect on a modulated Gaussian pulse passing through an SOA. Designing appropriate PhC-CDF to compensate for the nonlinear relation of amplitude to wavelength conversion by SOA, a high linear AO-ADC was achieved. However, the design was presented with a large footprint. To reduce the size of the device and the power consumption, we altered the structure by the integration of a line defect PhC waveguide into an SOA in this proposal. This integration has resulted in a new generation of SOAs that can be suitable for photonic integrated circuit design (Mizuta et al. 2006). It is worth noting that the use of a low-Δ W1-PhCW (i.e., a W1-PhCW with a small difference in its core and cladding relative refractive indices) results in the enhancement of the light-matter interaction near the photonic band edge, reducing the length of the PhC-SOA active region. This behavior makes this kind of SOAs (called PhC-SOAs) a new device suitable for use in Photonic integrated circuits (Taleb, Abedi 2014; Kotb et al. 2019, 2018; Kotb,Zoiros 2017; Kotb,Guo 2020). That is because the PhC-SOA medium shows higher nonlinear properties near the photonic band edge.

This paper presents a fully compact integrated 2-bit AO-ADC, consisting of a PhC-SOA as a nonlinear optical quantizer integrated with two PhC-CDFs. SPM in PhC-SOA induces a frequency

chirp in the input pulse due to its energy. Thus, an amplitude to wavelength conversion occurs which will be filtered by two PhC-CDFs. The PhC-CDFs are properly designed to quantize the signal into four bits. Integrating PhC-SOA with PhC-CDFs on an InP/InGaAsP/InP slab can lead to an ultrasmall-footprint high linear low power AO-ADC. We show that using PhC-SOA with a small constant group index has the advantage of designing higher bit resolution AO-ADCs with no missing code. The bit resolution can be improved by alternating the configuration of the high-quality factor PhC-CDFs.

In the next section, we describe the operating principles of the proposed integrated AO-ADC and design considerations. Section 3 presents the numerical model and the design procedure. Simulation results are presented in section 4. Finally, in Section 5 we conclude and propose future work directions.

2 The proposed Integrated AO-ADC

The operating principle of the proposed integrated AO-ADC is similar to those of the design presented by (Moshfe et al. 2020), such that an active region provides the medium for the SPM nonlinear effect occurrence. A modulated ultra-fast Gaussian pulse chain as an input optical signal, as schematically illustrated in Fig. 1a enters the PhC-SOA. The signal at the PhC-SOA output, due to the long gain recovery time, exhibits a frequency chirp that depends on the input pulse energy. Hence, an amplitude to wavelength conversion occurs. After passing through the PhC-CDFs, the chirped signal is quantized into a four-level coded signal. The PhC-CDFs are properly designed to produce the Gray-code (i.e., 00, 01, 11, and 10). To this aim, as we show in Section 4.1, the filter bandwidth (BW) determines the pulsewidth of the input pulse. Moreover, to code the shifted signal, the design is aimed to obtain the maximum possible shift for any given pulsewidth.

As schematically shown by Fig. 1b, the proposed integrated AO-ADC consisted of a PhC-SOA integrated with two PhC-CDFs, whose core regions are made of InGaAsP. The core regions are cladded by InP layers. All are devised on an array of holes with the radii of r=0.36a where a is the lattice constant in an InP/InGaAsP/InP slab. The core layer of the PhC-CDF platform is thicker than the PhC-SOA, as illustrated in Fig. 1b. To minimize the coupling loss for the optical signal crossing the interfaces between the PhC-SOA and the adjacent PhC-CDFs, a coupling region is considered at the interface which is integrated on the same air-hole PhC platform with the same hexagonal lattice. Since the PhC-CDFs are passive components, the larger thickness of GaInAsP set the dispersion of the signal to be sufficiently far from the band edge. The details of each component will be given in Section 4.

In comparison to (Moshfe et al. 2020), we substitute the conventional SOA and square-lattice pillar-based PhC-CDF with shorter length PhC-SOA and high-quality point defects PhC-CDF, all are devised on air-hole hexagonal-lattice based platform. These changes result in achieving an ultra-compact structure with the minimum optical loss between the blocks, operating with a small injection current.

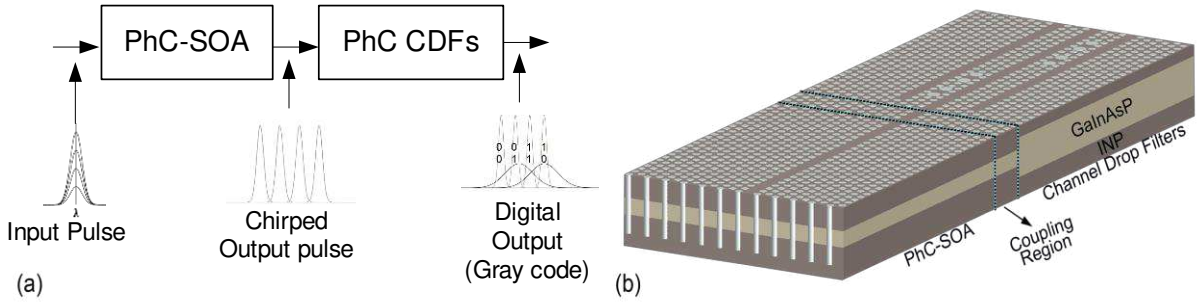

Fig. 1 (a) operating principle and (b) 3D schematic of the proposed structure

3 Numerical Model

The SOA frequency chirp, due to its long gain recovery time, is sensitive to the input pulse amplitude. Pulse propagation models in SOA (Agrawal, Olsson 1989; Razaghi et al. 2009; Nosratpour et al. 2018) has already been reported in the literature. Employing the model developed by (Agrawal, Olsson 1989), one can describe the dynamics of the PhC-SOA gain, g, power, P, and the spatial variation in the phase of the signal, ϕ, presented by Equations (1-3).

$$\frac{\partial g}{\partial \tau} = \frac{g_0 - g}{\tau_c} - \frac{n_r g P}{E_{\text{sat}}}; \quad \tau \equiv t - \frac{v_g}{z} \tag{1}$$

$$\frac{\partial P}{\partial z} = \left(n_r g - \alpha_{\text{int}}\right) \cdot P \tag{2}$$

$$\frac{\partial \phi}{\partial z} = -\frac{1}{2} n_r g \alpha \tag{3}$$

where z and t are the space and time coordinates, τ, τ_c, v_g, α_{int}, and α, are the spontaneous carrier lifetime, signal group velocity in the active medium, internal loss, and the linewidth enhancement factor, and $n_r=n_g/n_m$ where n_g and n_m are the group index and the equivalent modal index of a standard SOA, respectively.

Equation (1) presents the small-signal gain where Γ, a_N, N_0, I, are the confinement factor, gain coefficient, transparency carrier density, injection current, respectively. $I_0=qVN_0/\tau_c$ is the transparency injection current, in which, q and V are the electron charge and active layer volume.

$$g_0 = \Gamma a_N N_0 \left(I/I_0 - 1\right) \tag{4}$$

Equation (5) is the saturation energy, where ħ, ω_0, and $\sigma=V/L\Gamma$ are the reduced Planck's constant, pulse radian frequency, and the mode cross-section.

$$E_{\text{sat}} = \hbar\omega_0 \sigma/\alpha \tag{5}$$

In comparison with a conventional SOA ($\alpha_{int}\approx 0$), the internal loss of the PhC-SOA depends on the group index (Nosratpour et al. 2018),

$$\alpha_{\text{int}} = 325\exp\left(0.01529 n_g\right) - 393.6\exp\left(-0.1893 n_g\right) \tag{6}$$

For a given temporal Gaussian input pulse of energy E_{in} and time constant τ_0 that is related to the temporal pulsewidth τ_p by $\tau_p=2(2\ln 2)^{1/2}\tau_0$,

$$P_{\text{in}}(\tau) = \frac{E_{\text{in}}}{\tau_0\sqrt{\pi}} \exp\left(-\frac{\tau^2}{2\tau_0^2}\right). \tag{7}$$

after solving (1) and (2) numerically for P(t) and g(t), one can obtain the phase change, by (3), corresponding to a chirp in the output signal frequency,

$$\Delta\omega_{out} \equiv \frac{d\phi_{out}}{d\tau} \tag{8}$$

The corresponding chirp in the output wavelength is

$$\Delta\lambda_{out} \equiv -\frac{\lambda}{c}\frac{d\phi_{out}}{d\tau} \tag{9}$$

4 Design Procedure

The nonlinear property of PhC-SOA to convert the amplitude of the Gaussian pulse to wavelength shift is SPM which is related to the signal gain, energy, and the temporal pulsewidth. The signal gain and the frequency chirp in the pulse signal of a PhC-SOA, while compared with those in a conventional SOA, have been discussed in (Nosratpour et al. 2018). It has already been shown that in PhC-SOA, for an input temporal pulse of width τ_p, the larger the signal gain of the amplifying cavity, the larger the shift in the wavelength of the chirped signal ($\Delta\lambda_{out}$) (Nosratpour et al. 2018), similar to what examined in conventional SOAs (Moshfe et al. 2020). However, in PhC-SOA the wavelength shift depends on the group index too. (Nosratpour et al. 2018) demonstrated that the wavelength shift induced by the PhC-SOA is linearly dependent upon the group index (i.e., $\Delta\lambda_{out} \propto n_g$), provided the injection current is kept constant. Nonetheless, in PhC-SOA, keeping the gain constant will enhance the SPM property for a smaller n_g. However, $\Delta\lambda_{out}$ would never be equal for two different n_gs according to Equations (3) and (9), and a larger wavelength shift occurs for larger n_g. Consequently, we have to examine the frequency chirp in PhC-SOA for different values of group indices under the condition of keeping the signal gain constant. It would be possible, if we increase the injection current or the length of the device for smaller n_g. Hence, selecting n_g as large as possible results in decreasing the injection current and the input temporal pulsewidth. On the other hand, to provide a constant n_g for a band of wavelengths, we need to design a W1-PhCW with a constant-n_g dispersion to reduce the speed of pulse propagation. The range of flat band slow light (FBSL) depends on the value of the maximum wavelength shift required. This parameter is determined by the quality factor of the PhC-CDFs, as will be demonstrated in the next section. The FBSL is decreasing when n_g is increasing (Ebnali-Heidari et al. 2009). Hence, n_g is one of the critical design parameters that should be selected properly.

4.1 PhC-SOA Design

Figure 2a schematically shows the PhC-SOA as the major building block of the proposed AO-ADC which converts the intensity to wavelength. The design parameters for this block are based on experimental (Mizuta et al. 2006) and theoretical (Nosratpour et al. 2018) results. The substrate and the top cladding materials are InP, and the active (core) material is GaInAsP. The thicknesses of the top cladding and the core layers are h_{cl} and h_{co}, respectively. As shown in Fig. 2a, a hexagonal lattice of the period a is devised by punching a 2-D array of circular air-holes of depths h_h ($> h_{cl}+h_{co}$) and radii of r into the 3-layer structure. The geometrical and physical parameters are given in Table 1. The penetration of the PhC air-hole into a significant portion of the substrate considerably reduces the thermal resistance of the structure. A single line defect, forming a W1-PhCW for confining the optical signal with a small group velocity within the photonic band, aiming to enhance the optical gain through the SOA (Nosratpour et al. 2018).

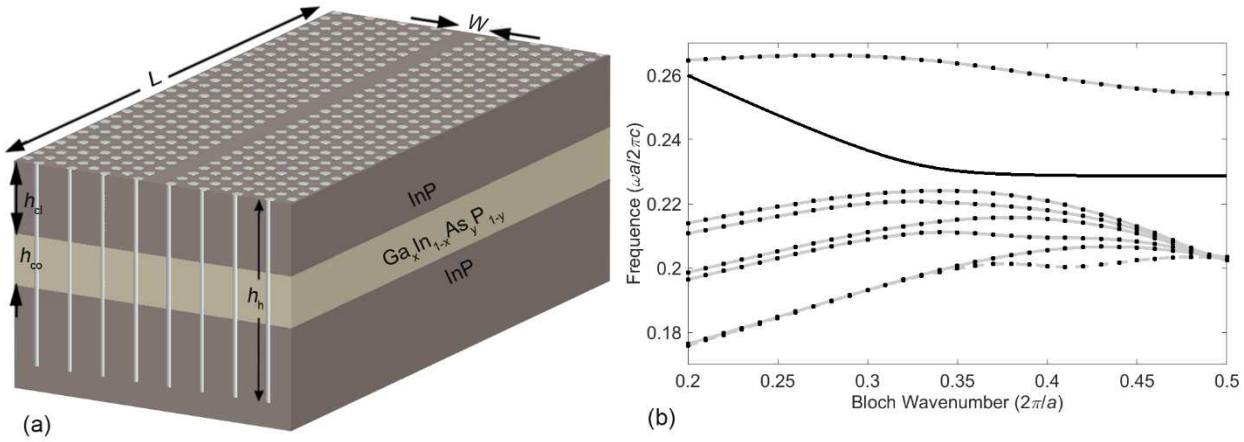

Fig. 2 (a) 3D schematic of the PhC-SOA and (b) the guided mode dispersion

The dispersion curve which is calculated by PWE in Rsoft as shown by Fig. 2b exhibits the normalized frequency range versus the wavenumbers for the structure given in Fig. 2a. There exists a single mode dispersion in the $0.23<a/\lambda<0.25$ interval. Near the band edge, the group index is increased and therefore the performance of a PhC-SOA is analogous to that of a conventional SOA with a shorter length (L), although with a large radiation loss.

Table 1 Parameters used in the simulation (Mizuta et al. 2006; Nosratpour et al. 2018)

Symbol	Quantity	Size	Units	Symbol
a	Lattice constant	350	nm	a
h_h	Air-hole height	5.62a	nm	h_h
h_{cl}	Top cladding layer thickness	1.58a	nm	h_{cl}
h_{co}	Active region (core) thickness	1.32a	nm	h_{co}
L	Active region length	9	μm	L
W	Active region width	1.372a	nm	W
n_{cl}	InP (cladding) refractive index	3.17	–	n_{cl}
n_{co}	GaInAsP (core) refractive index	3.45	–	n_{co}
a_N	Material gain constant	4×10^{-20}	m^2	a_N
I	Injection current	5.6	mA	I
N_0	Transparency carrier density	2×10^{23}	m^{-3}	N_0
n	Active region Modal refractive index	3.45	–	n
α	Linewidth enhancement factor	5	–	α
Γ	Optical confinement factor	0.191	–	Γ
λ	The signal center wavelength	1550	nm	**λ**
τ_C	Carrier lifetime in the active region	250	ps	τ_C

To design a PhC-SOA based AO-ADC using SPM nonlinearity, we must calculate the redshift induced by PhC-SOA for different values of n_g, given that the signal gain is kept constant. Hence, to simulate the dynamic behavior of the PhC-SOA as the nonlinear part of the integrated AO-ADC shown in Fig. 2a, the 2D finite difference time domain (FDTD) numerical method is employed where the code is written and simulated in MATLAB Consider the PhC-SOA shown in Fig. 2a, we employ the constant parameters given in Table 1. By solving (4) and (5) with the parameters

given in Table 1, E_{sat}= 3.72 pJ and g_0 = 319.53 $cm^{-1}$are obtained. These parameters lead to an unsaturated signal gain of 30 dB.

Figure 3a shows the shifts exhibited on the output wavelengths due to the phase changes induced by the PhC-SOA, for a Gaussian signal of pulsewidth τ_p=2, 4, 8, 12, and 20 ps, versus the pump energy for n_g=100, comparing one case (τ_p=2) with n_g=20, by varying the injection current (I=5.6mA for n_g=100 and I=24mA for n_g=20) to satisfy the constant gain condition. It is observed that if n_g=100, 5 times greater than n_g=20, the maximum wavelength shift decreases by a factor of 3. Thus, for a constant signal gain and the desired pulsewidth, for a greater n_g more wavelength shift occurs, resulting in a better signal coding. On the other hand, for n_g=20, the variation in $\Delta\lambda_{out}$ versus E_{in} becomes more linear (Fig. 3a). This is one of the advantages of PhC-SOA over the conventional SOAs for designing AO-ADCs. An ideal ADC produces the digital outputs for equal ranges of E_{in}. Therefore, the linear relation between $\Delta\lambda_{out}$ and E_{in} will facilitate designing a linear AO-ADC using similar PhC-CDFs without missing any code. One may use 2^n high quality factor PhC-CDFs to filter the chirped signal and digitize it into n-bit digital codes. However, this is not the major aim of this proposal.

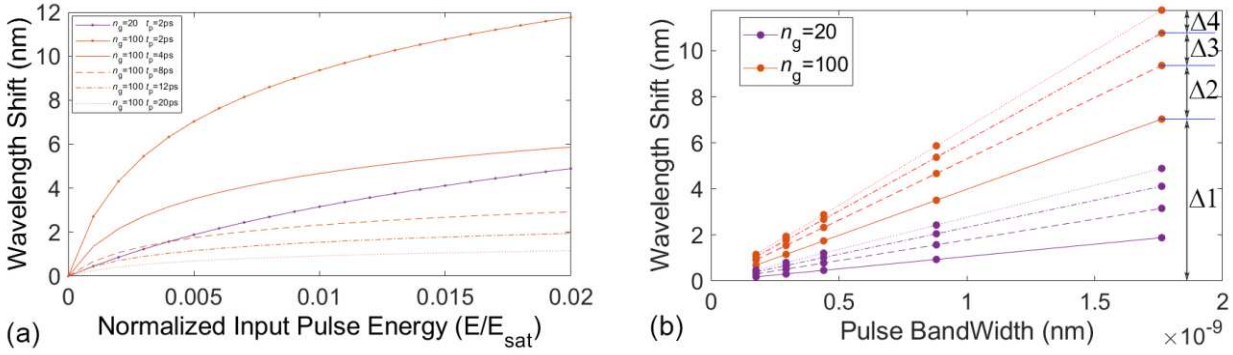

Fig. 3 The amount of wavelength shift versus (a) the pulse energy for n_g=100 and τ_p=2, 4, 8, 12, 20 ps, comparing with n_g=20 and τ_p=2; (b) the pulse bandwidth for n_g=20 and 100 for the energies E_{in}=0.005, 0.01, 0.015, and 0.02 E_{sat}.

As expected, the PhC-SOA SPM incurs a redshift on the output pulse signal that increases linearly with an increase in the input pulse bandwidth ($\Delta\lambda_{1/2}$) for different values of n_g, similar to conventional SOA (Moshfe et al. 2020). As shown in Fig. 3a, as an example, in the pulse energy of E_{in}=0.02E_{sat} the amount of redshift is almost 12 and 1.2 nm for τ_p=2 ps and τ_p=20ps respectively. The linear dependence at four given input energies of E_{in}=0.005E_{sat}, 0.01E_{sat}, 0.015E_{sat}, and 0.02E_{sat} (i.e. the threshold energies at them the digital outputs switch) are illustrated in Fig. 3b for n_g=20 (purple) and n_g=100 (red). This linear relation indicates that for the desired n_g, regardless of the temporal pulsewidth, $\Delta\lambda_{out}/\Delta\lambda_{1/2}$ ratio is more significant than the change in the input pulsewidth. Hence, to design the PhC-SOA based AO-ADC, similar to the SOA-based (Moshfe et al. 2020), the signal pulsewidth will be determined due to the maximum wavelength shift needed. Fig. 3b illustrates for n_g=100 and τ_p=2ps, the amount of wavelength shift Δ_i (i=1, 2, 3, and 4) for four equal ranges of energies. Clearly for n_g=20, the differences between Δ_is are smaller, confirming more linear relation between $\Delta\lambda_{out}$ and E_{in} for smaller n_g.

As discussed above, for a desired temporal pulsewidth, there is a more linear dependence between $\Delta\lambda_{out}$ and E_{in} for a smaller n_g. Although this linearity is very important, a novel method is considered to compensate for this nonlinear relation (Moshfe et al. 2020) which is useful for

designing 2-bit AO-ADCs. The compensation scheme is shown in Fig. 4, the bandpass filters should be designed in such a way that they would compensate for the nonlinear relation between $\Delta\lambda_{out}$ and E_{in}. To this aim, two PhC-CDFs can be designed such that the wavelength distances between their cross point at the threshold T=50% be equal to Δ_is.

By properly designing the PhC-CDFs, the nonlinearity that occurs for larger n_gs will not pose a major problem on the final design nonlinearity errors. To design a 2-bit AO-ADC, this method would decrease the nonlinearity errors. Whereas for increasing the resolution bits, other methods should be considered. However, the lesser nonlinear relation of $\Delta\lambda_{out}$ and E_{in} in PhC-SOA (for smaller n_g) makes them preferable compared to conventional SOA for higher resolution bit AO-ADC, if no compensation methods are used.

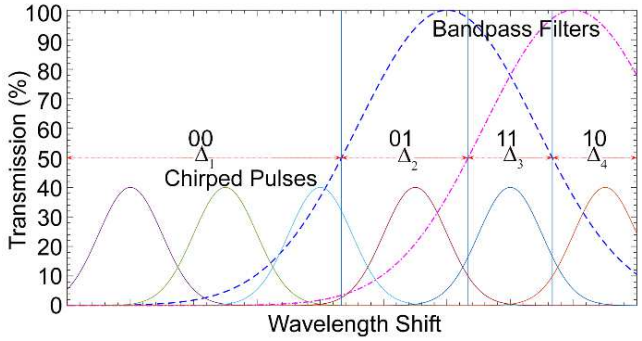

Fig. 4 The two PhC-CDFs transmission spectra to compensate for the nonlinear relation of $\Delta\lambda_{out}$ and E_{in} in PhC-SOA

Fig. 4 indicates that the maximum wavelength shift depends on the Full width at half the maximum of PhC-CDF ($FWHM_{CDF}$). To determine the maximum wavelength shift required for the desired group index and $FWHM_{CDF}$, given $R_i=\Delta_i/\Delta_2$ (i=1,3,4) and $FWHM_{CDF}= \Delta_2+\Delta_3$, we obtain Equation (10).

$$\text{Max Shift} = \Delta 1 + \Delta 2 + \Delta 3 + \Delta 4 = \frac{1+R1+R3+R4}{1+R3}.\text{FWHM}_{CDF} \quad (10)$$

In PhC-SOA, the ratios Δ_i/Δ_j (i,j=1, 2, 3, 4) are almost the same for any given input pulsewidth for a definite n_g because of the linear relation between $\Delta\lambda_{out}$ and $\Delta\lambda_{1/2}$ (Fig. 3b). Therefore, we can calculate those ratios by finding the corresponding redshifts ($\Delta_{1,2,3,4}$) for different values of n_g which are represented as examples of four quantization levels of a 4-level quantization scheme shown in Table 2; given τ_p=10 ps and dividing the input energy range $0 \le E_{in}/E_{sat} \le 0.02$ into for equal steps ($\Delta E_{in}/E_{sat}$=0.005).

Table 2 examples of 4 level quantization for different values of n_g and τ_p = 10ps

Range of ΔE_{in} ($0.01E_{sat}$)		0.0→0.5	0.5→1	1→1.5	1.5→2
$\Delta\lambda_{out}$ (nm)	n_g=20	0.371	0.2524	0.2904	0.1536
	n_g=40	0.6778	0.3592	0.241	0.182
	n_g=60	0.8979	0.4041	0.26	0.192
	n_g=80	1.159	0.44	0.275	0.197
	n_g=100	1.393	0.464	0.28	0.2
Gray Code		00	01	11	10
Decimal Value		0	1	2	3

The ratios of R_i for the given n_gs are given in Table 3.

Table 3 The amounts of $R_i=\Delta_i/\Delta_2$ for different values of n_g

Ratios	n_g=20	n_g=40	n_g=60	n_g=80	n_g=100
$R_1= \Delta_1/ \Delta_2$	1.47	1.885	2.22	2.635	3
$R_3= \Delta_3/ \Delta_2$	0.755	0.671	0.645	0.625	0.603
$R_4= \Delta_4/ \Delta_2$	0.61	0.505	0.475	0.447	0.431

As demonstrated above, to find the temporal pulsewidth, we have to find the maximum value of n_g possible. Therefore, we have to calculate the amount of FBSL and compare it to the maximum wavelength shift required for different values of n_g. Then, for a certain n_g, the temporal pulsewidth will be determined to achieve that maximum wavelength shift.

4.2 Channel drop filter design

As represented by Equation (10), the maximum wavelength shift required for determining the signal pulsewidth is a function of $FWHM_{CDF}$. Designing highly selective reflectors using ring resonators leads to smaller wavelength shift; yet, they occupy large areas, the single defect cavity resonator which is shown in Fig. 5a is designed by removing one hole between two waveguides and varying the radii of two adjacent air holes (r_b) (Fan et al. 1999; Olyaee, Najafgholinezhad 2013). Recalling that the core layer of this block is much thicker than the PhC-SOA to locating the dispersion sufficiently far from the band edge. The radii of the air holes beside the omitted air hole tune the resonance frequency of the defect cavity. To improve the transmission, we consider two-point defects with phase matching, i.e., $k_x d=n\pi+\pi/2$. To this aim, the distance between the point defects must be d=5a. In Fig. 5b, the transmission coefficient versus the wavelength is illustrated. The resonance wavelength and the PhC-CDF $FWHM_{CDF}$ are 1552 and 0.6 nm for a=350 nm and r_b=0.75r=94.5nm. In Fig. 5c, applying a continuous wave signal with λ=1.552μm, the time evolution of the output port is depicted.

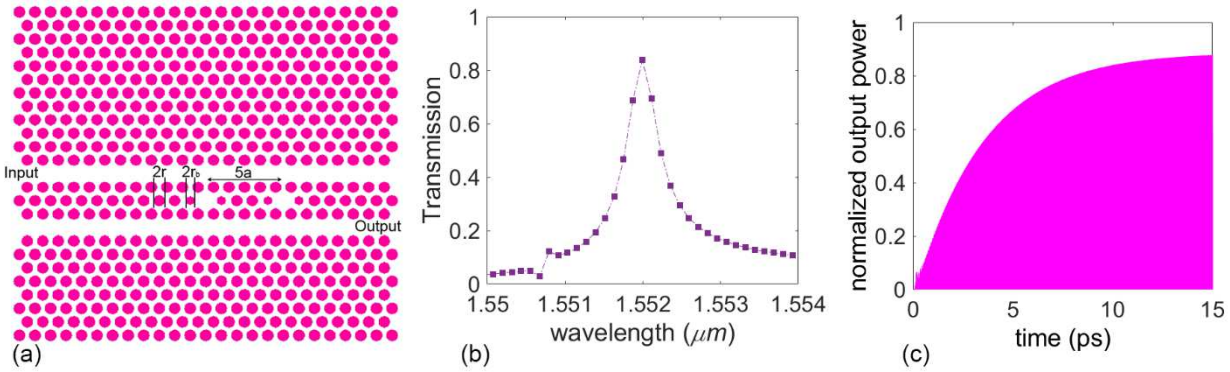

Fig. 5 PhC-CDF (a) schematic, (b) transmission spectra, and (c) its time evolution at the resonance wavelength

4.3 Flat Band Slow Light Design

To design a working structure properly, we need an FBSL for the active region. Since the FBSL has a reverse relationship to n_g, this factor plays an important role in finding the values of n_g.

Among all the method used to achieve a nearly constant n_g, such as the variation of the air-holes dimensions (Kubo et al. 2007) and configuration (Säynätjoki et al. 2007), we used the microfluidic infiltration which takes the advantage of its post-fabrication tunability (Bitarafan et al. 2011) with minimal fabrication errors. To provide the FBSL for the active region, we infiltrated the adjacent rows of the line defect with various commercial liquids of n_f=1.3-1.7 (Speciality optical liquids 2020). Calculating the band diagram by the PWE method and using $n_g=c/v_g=c.dk/d\omega$, the values of n_g for different amounts of n_f versus the normalized frequency are calculated as presented by Fig. 6a.

In Fig. 6b, the values of FBSL bandwidth with the tolerance of ±5% for a=350nm versus the values of n_g are shown. On the other hand, the maximum shift required for $FWHM_{CDF}$=0.6nm according to Equation (10) and Table 3 is also drawn. The cross point (n_g=70) declares the maximum value of n_g that we can use. This value is the greatest value of n_gs. The greater values of n_g have advantages such as more wavelength shift induced by PhC-SOA for a shorter length and smaller injection current.

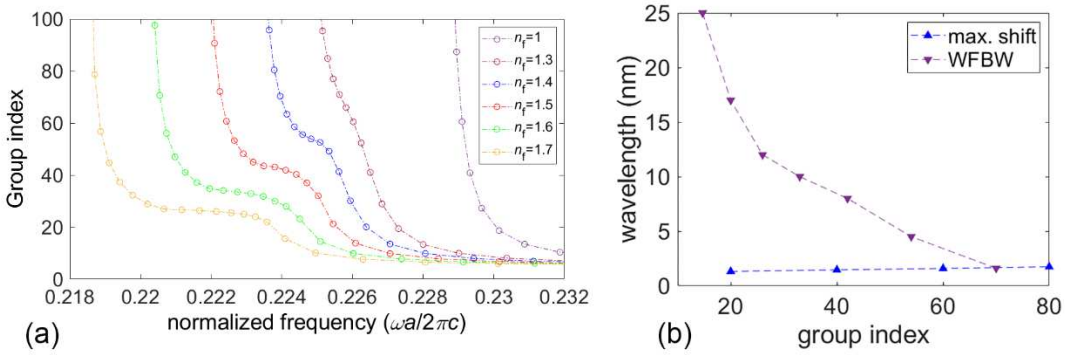

Fig. 6 (a) n_g versus the normalized frequency for different values of microfluidic infiltration; (b) the maximum shift required and the FBSL bandwidth for different values of n_g

5 PhC-SOA based AO-ADC

The proposed PhC-SOA based AO-ADC is illustrated in Fig. 7. It consists of three parts including PhC-SOA, two PhC-CDFs, and the coupling region that works as an interconnect between the PhC-SOA and two PhC-CDFs.

Infiltrating the adjacent rows of the active waveguide in the PhC-SOA with n_{f1}=1.35 (red holes) leads to the values of n_g versus the wavelength as shown in Fig. 8a. It is observed that a nearly constant n_g=60 is obtained for 1.55<λ<1.554. As mentioned earlier, the thicker core layer of the slab, on which the PhC-CDFs is designed, makes this range of wavelength be far away from the band edge. To minimize the coupling loss between the active and passive waveguides with the constant n_g=5, we used step by step changing in group index (Hosseinpour et al. 2013). Thus, at the junction of PhC-SOA and PhC-CDFs, the adjacent rows filled with the liquid with n_{f2}=1.5 (blue holes) and n_{f3}=1.6 (purple holes). According to Equation (11) the calculated coupling loss is less than 50% since n_g decreased step by step from 60 to 40, 40 to 20, and 20 to 5. The values of n_g are derived from Fig. 6a for the normalized frequency of a/λ=0.2255 where a=350nm and λ=1.552μm. Without this region, the loss would be more than 70%.

$$\eta = \frac{4n_{g1}n_{g2}}{(n_{g1}+n_{g2})^2} \tag{11}$$

For the achieved nearly constant n_g, according to the Ratios of R_1, R_2, and R_3 for n_g=60 and $FWHM_{CDF}$=0.6nm, by Equation (10), the maximum shift required will be $\Sigma\Delta_i$~1.652nm. Therefore, the values of Δ_1=0.865nm, Δ_2=0.393nm, Δ_3=0.207nm, Δ_4=0.187nm are obtained.

To achieve the required wavelength shift incurred on the input Gaussian pulse, by setting the injection current I=8.5mA, the number of wavelength shifts versus the energy for τ_p=10.6ps will be 1.652 nm that is illustrated in Fig. 8(b).

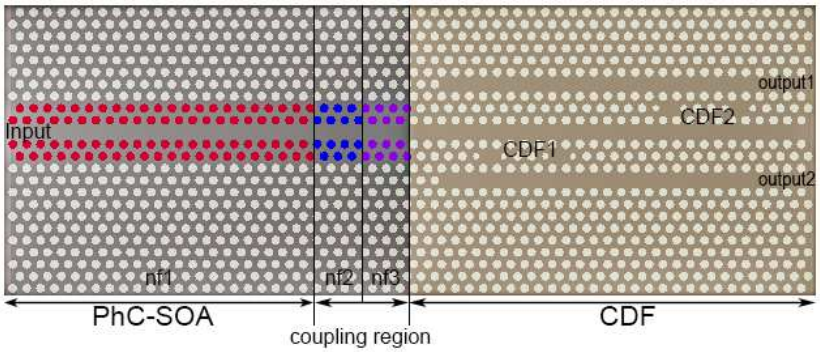

Fig. 7 The proposed AO-ADC

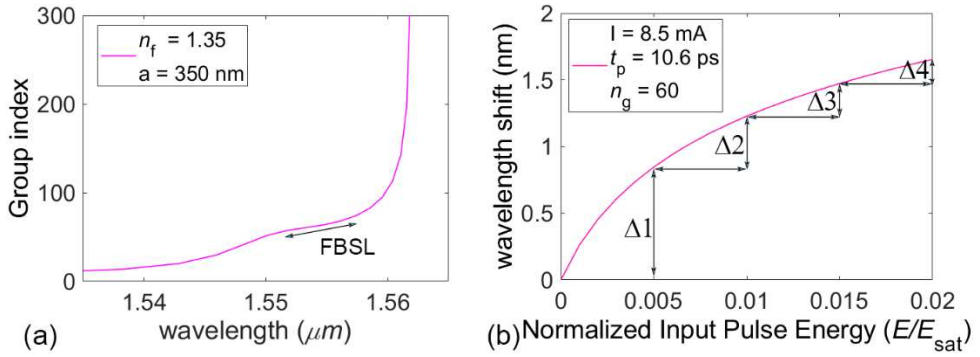

Fig. 8 n_g versus the wavelength for n_f=1.35, and the amount of FBSL bandwidth for n_g=60, (b) the amount of wavelength shift for n_g=60

By setting r_{b1}=0.736r and r_{b2}=0.75r, the two PhC-CDFs with the transmission spectra shown in Fig. 9 are designed to be capable of properly coding the chirped signal. In Fig. 9, considering T = 42% as the boundary between logical 0 and 1, the threshold for quantization levels at λ=1551.7, 1552.093, and 1552.3nm are illustrated.

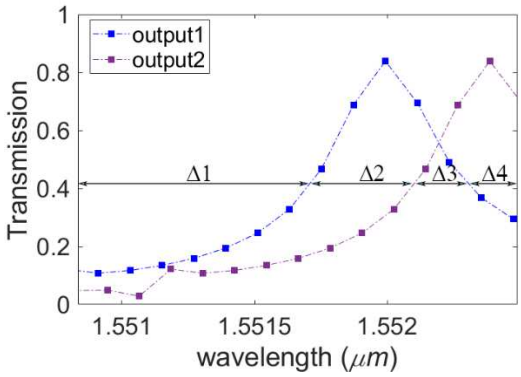

Fig. 9 PhC-CDF output versus the wavelength compatible with coding the chirped signal with the characteristic shown in Fig. 8(b)

To calculate the maximum speed of the AO-ADC, we should consider the time response of the PhC-CDF and the gain/phase recovery time of the PhC-SOA. From Fig. 5c, we can estimate that the output settling time is 10ps, while the PhC-SOA recovery time is calculated 100ps. Thus, the AO-ADC speed is limited by PhC-SOA recovery time. Although there are several methods to decrease the recovery time, according to this factor, the speed of the proposed AO-ADC will be 10GSample/s.

Launching 10Gs/s continuous chains of 10.6-ps Gaussian pulses with the same center wavelength (λ=1551.228nm) with different energies ($0<E_{in}/E_{sat}<0.02$) four digital state of the AO-ADC output are examined. The simulation results show that the wavelength shifts incurred on the input pulses of given energies, by the PhC-SOA, coincide with those of Fig. 8b, resulting in different pulses with shifted center wavelengths. Then, the PhC-CDF outputs code these pulses digitally as desired. In Fig. 10a, normalized output power and equivalent binary codes (assuming T = 42%) are shown. From this figure, the integral and differential nonlinearity (INL/DNL) errors corresponding to each digital state can be calculated. The INL and DNL errors in terms of the least significant bit (LSB), corresponding to four digital states are shown in Fig. 10b. The maxima for DNL and INL errors are 0.2 and 0.12 LSB corresponding to state three.

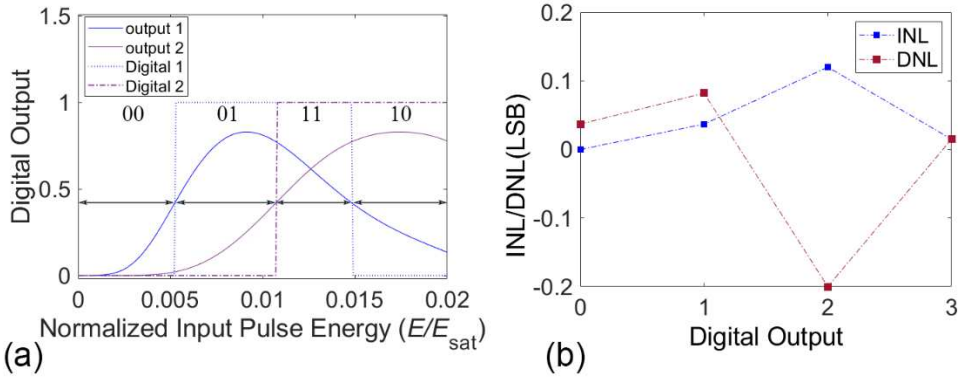

Fig. 10 Normalized output power and the relative digital outputs versus the input pulse energy; (b) INL and DNL errors for each binary state

Finally, we compare the parameters obtained for the proposed AO-ADC with all the other AO-ADC structures reported in the past decades, as tabulated in Table 4. Among these, the SOA and

PhC-based AO-ADCs are integrable, while the fiber-based can generate more quantization levels (QL). The power reported in this table is the input analog optical power and does not relate to what the ADC structure consumes. The PhC-based AO-ADCs do not need any power supplies and operate in the presence of input signals, while SOA-based AO-ADCs power consumption depends on the numbers of the SOAs used. For example, in (Scaffardi et al. 2009) and (Wen et al. 2012), five and three SOAs are used to design 2-bit and 3-bit AO-ADCs, while in the present work a single SOA used that indicates this design has less overall power consumption. Although just an SOA is used in (Hoshino et al. 2018) and (Moshfe et al. 2020), our structure presents the advantages of consuming a smaller injection current (6.5mA vs 1200mA (Hoshino et al. 2018) and 75mA (Moshfe et al. 2020)) and smaller footprint. To compare with PhC based AO-ADCs, the proposed structure is more linear, since there is no way to design PhC nonlinear structures to digitize the analog signal linearly. As shown in Table 4, there is no information about the nonlinearity errors in those references (Youssefi et al. 2012; Xin, Linfeng 2020; Shamsi, Moradi 2020; Sani et al. 2020b; Mehdizadeh et al. 2017a, b, c; Khosroabadi et al. 2020; Jafari et al. 2018; Baghbanzadeh, Andalib 2020). Even though they are comparable with our work from the structure occupation area view, they cannot perform the conversion linearly. However, this structure has the smallest footprint among all the reported PhC-based AO-ADCs, except (Jafari et al. 2018). In PhC-based AO-ADCs, improving the bit resolution is not possible either, since the mechanism and the signal power limit these structures to increase the quantization levels.

For the future, the researcher can work on increasing the output of digital bits of the proposed structure. To do so, one may use the higher quality factor PhC-CDFs. To obtain linear AO-ADC, small n_g or PhC-CDF with tunable FWHM to compensate the nonlinear frequency chirp induced by Ph-SOA should be considered.

Table 4 Comparison of parameters for various Optical AO-ADCs

ADC	Speed (Gs/s)	QL (bit)	Power (mW)	Footprint (μm^2)	INL (LSB)	DNL (LSB)	Ref
HNLF	40	64	N/A	−	N/A	N/A	(Xu, Liu 2003)
HNLF	N/A	3	10.5	−	N/A	N/A	(Nishitani et al. 2005)
DFF[b]	40	4	2560	−	N/A	N/A	(Oda, Maruta 2005)
ADF/ZDF[c]	160	4	1200/600	−	N/A	N/A	(Oda, Maruta 2006)
HNLF	100	16	33500	−	N/A	N/A	(Nishitani et al. 2008)
HNLF	40	32	45	−	0.875	0.75	(Konishi et al. 2011)
PCF[d]	N/A	6	375	−	N/A	N/A	(Zhe et al. 2013)
HNLF	40	16	200	−	0.4	0.5	(Nagashima et al. 2017)
SOA	20	4	8	N/A	N/A	N/A	(Scaffardi et al. 2009)
SOA	×100	8	4.8	N/A	0.7	0.4	(Wen et al. 2012)
QDSOA	10	8	10.5	N/A	0.5	0.7	(Hoshino et al. 2018)
SOA-PhC	10	4	10	12000	0.2	0.2	(Moshfe et al. 2020)
PhC	45	5	60/μm^2	N/A	N/A	N/A	(Youssefi et al. 2012)
PhC	200	4	16/mm^2	924	N/A	N/A	(Mehdizadeh et al. 2017a)
PhC	52	4	100/μm^2	806	N/A	N/A	(Mehdizadeh et al. 2017b)
PhC	77	4	100/μm^2	1520	N/A	N/A	(Mehdizadeh et al. 2017c)
PhC	1000	4	>25	42	N/A	N/A	(Jafari et al. 2018)
PhC	300	4	10000/μm^2	240	N/A	N/A	(Khosroabadi et al. 2020)
PhC	220	4	2000/μm^2	777.52	N/A	N/A	(Sani et al. 2020b)
PhC	250	4	3100/mm^2	2016	N/A	N/A	(Xin,Linfeng 2020)
PhC	260	4	1000/μm^2	540	N/A	N/A	(Sani et al. 2020a)

PhC	500	4	2000/μm^2	400	N/A	N/A	(Baghbanzadeh,Andalib 2020)
PhC	250	4	4000/μm^2	N/A	N/A	N/A	(Shamsi,Moradi 2020)
PhC-SOA	10	4	7	172	0.12	0.2	Present.

[a] high nonlinear fiber; [b] dispersion flattened fiber; [c] anomalous/zero-dispersion fiber; [d] photonic crystal fiber

6 Conclusion

By integrating an InP/InGaAsP/InP PhC-SOA with two point-defect PhC-CDFs devised on the same PhC slab with different core layer thickness, we designed a high linear ultra-low-power integrated AO-ADC with a small footprint. The proposed structure can convert 10.6ps amplitude modulated Gaussian pulses of center wavelengths 1551.228nm and energies ≤0.0744pJ into four coded digital output levels at 10Gs/s. The self-phase modulation effect in a short-length PhC-SOA, due to its long gain recovery time, induces frequency chirps, depending on the pulse energy. The two bandpass PhC-CDFs designed on the same hexagonal lattice connecting the PhC-SOA with an appropriately coupling region are designed to digitize and code the shifted signals, leading to the Gray code (00, 01, 11, and 10). Designing appropriate PhC-CDFs according to the range of redshifts, we have obtained the key element of this structure to be as linear as it can. The proposed design can be developed to have more quantization levels as a new generation of integrated AO-ADCs.

Declarations

Not applicable.

References

Agrawal, G.P., Olsson, N.A.: Self-phase modulation and spectral broadening of optical pulses in semiconductor laser amplifiers. IEEE Journal of quantum electronics **25**(11), 2297-2306 (1989)

Baghbanzadeh, M., Andalib, A.: A novel proposal for PhC-based OADC for Gray code generation. Photonics and Nanostructures-Fundamentals and Applications, 100847 (2020)

Bitarafan, M., Moravvej-Farshi, M., Ebnali-Heidari, M.: Proposal for postfabrication fine-tuning of three-port photonic crystal channel drop filters by means of optofluidic infiltration. Applied Optics **50**(17), 2622-2627 (2011)

Brzozowski, L., Sargent, E.H.: All-optical analog-to-digital converters, hardlimiters, and logic gates. Journal of Lightwave Technology **19**(1), 114-119 (2001). doi:10.1109/50.914492

Ebnali-Heidari, M., Grillet, C., Monat, C., Eggleton, B.: Dispersion engineering of slow light photonic crystal waveguides using microfluidic infiltration. Optics express **17**(3), 1628-1635 (2009)

Fan, S., Villeneuve, P.R., Joannopoulos, J., Khan, M., Manolatou, C., Haus, H.: Theoretical analysis of channel drop tunneling processes. Physical Review B **59**(24), 15882 (1999)

Hoshino, H., Okada, T., Matsuura, M.: Photonic analog-to-digital conversion using a red frequency chirp in a semiconductor optical amplifier. Optics Letters **43**(10), 2272-2275 (2018)

Hosseinpour, M., Ebnali-Heidari, M., Kamali, M., Emami, H.: Optofluidic photonic crystal slow light coupler. JOSA B **30**(3), 717-722 (2013)

Jafari, D., Nurmohammadi, T., Asadi, M.J., Abbasian, K.: All-optical analog-to-digital converter based on Kerr effect in photonic crystal. Optics & Laser Technology **101**, 138-143 (2018)

Jeong, J.-M., Marhic, M.: All-optical analog-to-digital and digital-to-analog conversion implemented by a nonlinear fiber interferometer. Optics communications **91**(1-2), 115-122 (1992)

Khosroabadi, S., Shokouhmand, A., Marjani, S.: Full optical 2-bit analog to digital converter based on nonlinear material and ring resonators in photonic crystal structure. Optik **200**, 163393 (2020)

Konishi, T., Takahashi, K., Matsui, H., Satoh, T., Itoh, K.: Five-bit parallel operation of optical quantization and coding for photonic analog-to-digital conversion. Optics express **19**(17), 16106-16114 (2011)

Kotb, A., Guo, C.: Numerical modeling of photonic crystal semiconductor optical amplifiers-based 160 Gb/s all-optical NOR and XNOR logic gates. Optical and Quantum Electronics **52**(2), 89 (2020)

Kotb, A., Zoiros, K.E.: Performance analysis of all-optical XOR gate with photonic crystal semiconductor optical amplifier-assisted Mach–Zehnder interferometer at 160 Gb/s. Optics Communications **402**, 511-517 (2017)

Kotb, A., Zoiros, K.E., Guo, C.: 160 Gb/s photonic crystal semiconductor optical amplifier-based all-optical logic NAND gate. Photonic Network Communications **36**(2), 246-255 (2018)

Kotb, A., Zoiros, K.E., Guo, C.: Ultrafast performance of all-optical AND and OR logic operations at 160 Gb/s using photonic crystal semiconductor optical amplifier. Optics & Laser Technology **119**, 105611 (2019)

Kubo, S., Mori, D., Baba, T.: Low-group-velocity and low-dispersion slow light in photonic crystal waveguides. Optics Letters **32**(20), 2981-2983 (2007)

Mehdizadeh, F., Soroosh, M., Alipour-Banaei, H., Farshidi, E.: All optical 2-bit analog to digital converter using photonic crystal based cavities. Optical and Quantum Electronics **49**(1), 38 (2017a)

Mehdizadeh, F., Soroosh, M., Alipour-Banaei, H., Farshidi, E.: A novel proposal for all optical analog-to-digital converter based on photonic crystal structures. IEEE Photonics Journal **9**(2), 1-11 (2017b)

Mehdizadeh, F., Soroosh, M., Alipour-Banaei, H., Farshidi, E.: Ultra-fast analog-to-digital converter based on a nonlinear triplexer and an optical coder with a photonic crystal structure. Applied Optics **56**(7), 1799-1806 (2017c)

Mizuta, E., Watanabe, H., Baba, T.: All semiconductor low-Δ photonic crystal waveguide for semiconductor optical amplifier. Japanese Journal of Applied Physics **45**(8R), 6116 (2006)

Moshfe, S., Moravvej-Farshi, M.K., Abedi, K.: Designing an Integrated All-Optical Analog to Digital Converter. International Journal of Optics and Photonics **14**(1), 3-14 (2020)

Nagashima, T., Hasegawa, M., Konishi, T.: 40 GSample/s all-optical analogs to digital conversion with resolution degradation prevention. IEEE Photonics Technology Letters **29**(1), 74-77 (2017)

Nathawad, L.Y., Urata, R., Wooley, B.A., Miller, D.A.B.: A 40-GHz-bandwidth, 4-bit, time-interleaved A/D converter using photoconductive sampling. IEEE Journal of Solid-State Circuits **38**(12), 2021-2030 (2003). doi:10.1109/JSSC.2003.819172

Nishitani, T., Konishi, T., Itoh, K.: Integration of a proposed all-optical analog-to-digital converter using self-frequency shifting in fiber and a pulse-shaping technique. Optical review **12**(3), 237-241 (2005)

Nishitani, T., Konishi, T., Itoh, K.: Resolution improvement of all-optical analog-to-digital conversion employing self-frequency shift and self-phase-modulation-induced spectral compression. IEEE Journal of Selected Topics in Quantum Electronics **14**(3), 724-732 (2008)

Nosratpour, A., Razaghi, M., Darvish, G.: Computational study of pulse propagation in photonic crystal semiconductor optical amplifier. Journal of Nanophotonics **12**(3), 036015 (2018)

Oda, S.-i., Maruta, A.: A novel quantization scheme by slicing supercontinuum spectrum for all-optical analog-to-digital conversion. IEEE Photonics Technology Letters **17**(2), 465-467 (2005)

Oda, S., Maruta, A.: Two-bit all-optical analog-to-digital conversion by filtering broadened and split spectrum induced by soliton effect or self-phase modulation in fiber. IEEE Journal of selected topics in Quantum Electronics **12**(2), 307-314 (2006)

Olyaee, S., Najafgholinezhad, S.: Computational study of a label-free biosensor based on a photonic crystal nanocavity resonator. Applied Optics **52**(29), 7206-7213 (2013)

Parandin, F., Kamarian, R., Jomour, M.: A novel design of all optical half-subtractor using a square lattice photonic crystals. Optical and Quantum Electronics **53**(2), 1-10 (2021)

Parandin, F., Karkhanehchi, M.M.: Terahertz all-optical NOR and AND logic gates based on 2D photonic crystals. Superlattices and Microstructures **101**, 253-260 (2017)

Razaghi, M., Ahmadi, V., Connelly, M.J.: Comprehensive finite-difference time-dependent beam propagation model of counterpropagating picosecond pulses in a semiconductor optical amplifier. Journal of Lightwave Technology **27**(15), 3162-3174 (2009)

Sani, M.H., Khosroabadi, S., Nasserian, M.: High performance of an all-optical two-bit analog-to-digital converter based on Kerr effect nonlinear nanocavities. Applied Optics **59**(4), 1049-1057 (2020a)

Sani, M.H., Khosroabadi, S., Shokouhmand, A.: A novel design for 2-bit optical analog to digital (A/D) converter based on nonlinear ring resonators in the photonic crystal structure. Optics Communications **458**, 124760 (2020b)

Säynätjoki, A., Mulot, M., Ahopelto, J., Lipsanen, H.: Dispersion engineering of photonic crystal waveguides with ring-shaped holes. Optics Express **15**(13), 8323-8328 (2007)

Scaffardi, M., Lazzeri, E., Fresi, F., Poti, L., Bogoni, A.: Analog-to-digital conversion based on modular blocks exploiting cross-gain modulation in semiconductor optical amplifiers. IEEE Photonics Technology Letters **21**(8), 540-542 (2009)

Shamsi, A., Moradi, R.: All optical analog to digital converter using nonlinear photonic crystal ring resonators. Optical and Quantum Electronics **52**(10), 435 (2020). doi:10.1007/s11082-020-02541-z

Speciality optical liquids. https://www.cargille.com/wp-content/uploads/2020/01/2020-Specialty-Liquids-Catalog.pdf (2020).

Taleb, H., Abedi, K.: Ultrafast all-optical signal processing using optically pumped QDSOA-based Mach–Zehnder interferometers. IEEE Journal of Selected Topics in Quantum Electronics **19**(5), 1-8 (2013)

Taleb, H., Abedi, K.: Design of a low-power all-optical NOR gate using photonic crystal quantum-dot semiconductor optical amplifiers. Optics Letters **39**(21), 6237-6240 (2014)

Taylor, H., Taylor, M., Bauer, P.: Electro-optic analog-to-digital conversion using channel waveguide modulators. Applied Physics Letters **32**(9), 559-561 (1978)

Wen, H., Wang, H., Ji, Y.: All-optical quantization and coding scheme for ultrafast analog-to-digital conversion exploiting polarization switches based on nonlinear polarization rotation in semiconductor optical amplifiers. Optics Communications **285**(18), 3877-3885 (2012)

Xin, G., Linfeng, Z.: All-optical analog to digital converter based on nonlinear photonic crystal ring resonators. Photonics and Nanostructures-Fundamentals and Applications, 100817 (2020)

Xu, C., Liu, X.: Photonic analog-to-digital converter using soliton self-frequency shift and interleaving spectral filters. Optics Letters **28**(12), 986-988 (2003)

Yang, S., Wang, C., Chi, H., Zhang, X., Zheng, S., Jin, X., Yao, J.: Photonic analog-to-digital converter using Mach-Zehnder modulators having identical half-wave voltages with improved bit resolution. Applied Optics **48**(22), 4458-4467 (2009)

Youssefi, B., Moravvej-Farshi, M.K., Granpayeh, N.: Two-bit all-optical analog-to-digital converter based on nonlinear Kerr effect in 2D photonic crystals. Optics communications **285**(13-14), 3228-3233 (2012)

Zhe, K., Jin-Hui, Y., Sha, L., Song-Lin, X., Bin-Bin, Y., Xin-Zhu, S., Chong-Xiu, Y.: Six-bit all-optical quantization using photonic crystal fiber with soliton self-frequency shift and pre-chirp spectral compression techniques. Chinese Physics B **22**(11), 114211 (2013)

Figures

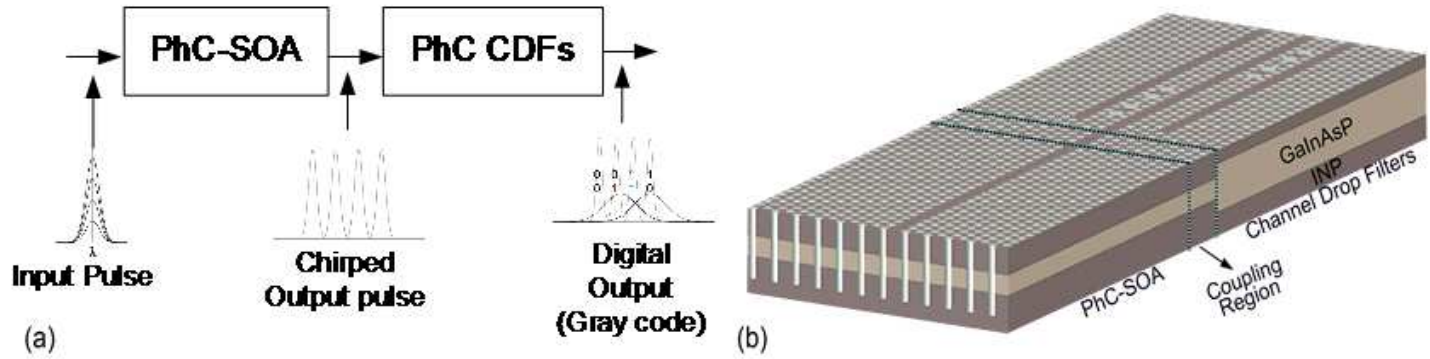

Figure 1

(a) operating principle and (b) 3D schematic of the proposed structure

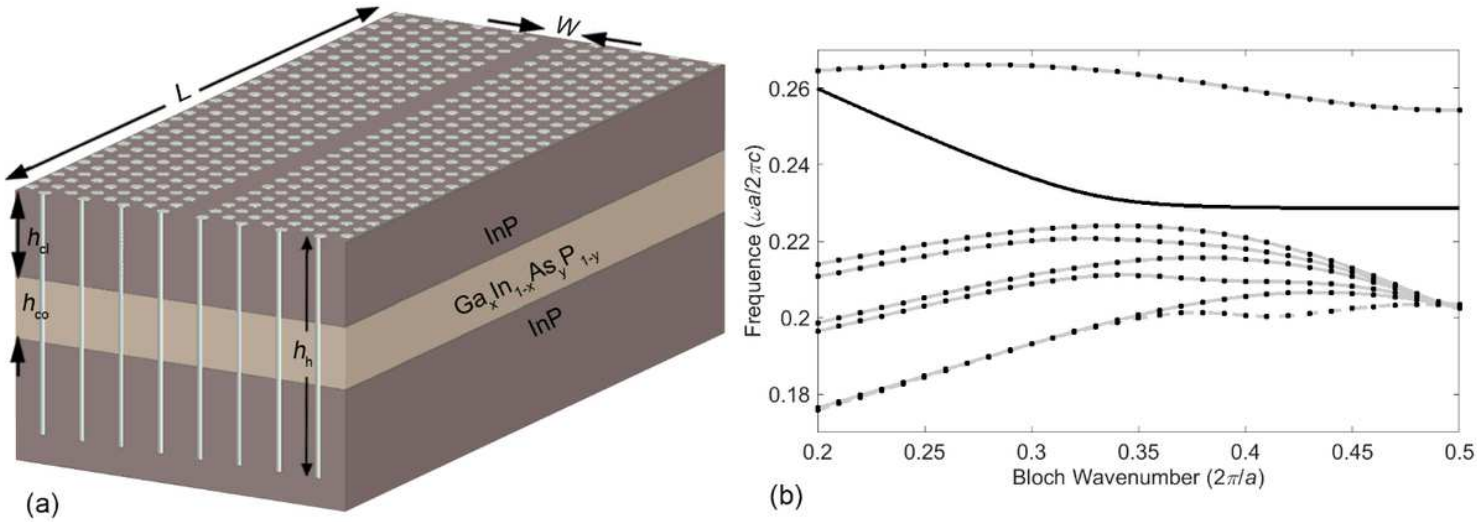

Figure 2

(a) 3D schematic of the PhC-SOA and (b) the guided mode dispersion

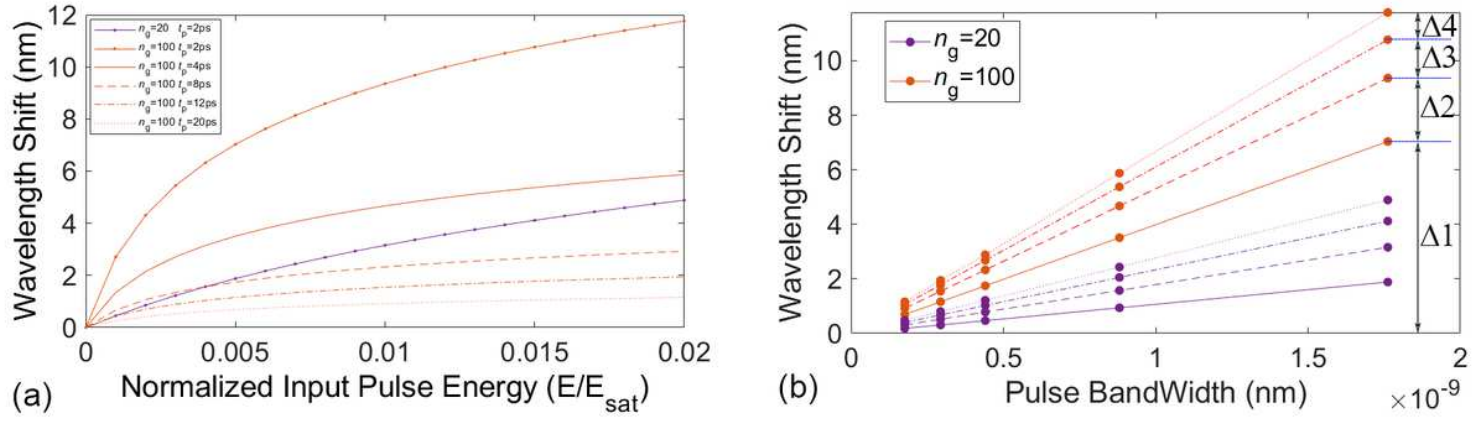

Figure 3

The amount of wavelength shift versus (a) the pulse energy for ng=100 and τp=2, 4, 8, 12, 20 ps, comparing with ng=20 and τp=2; (b) the pulse bandwidth for ng=20 and 100 for the energies Ein=0.005, 0.01, 0.015, and 0.02 Esat.

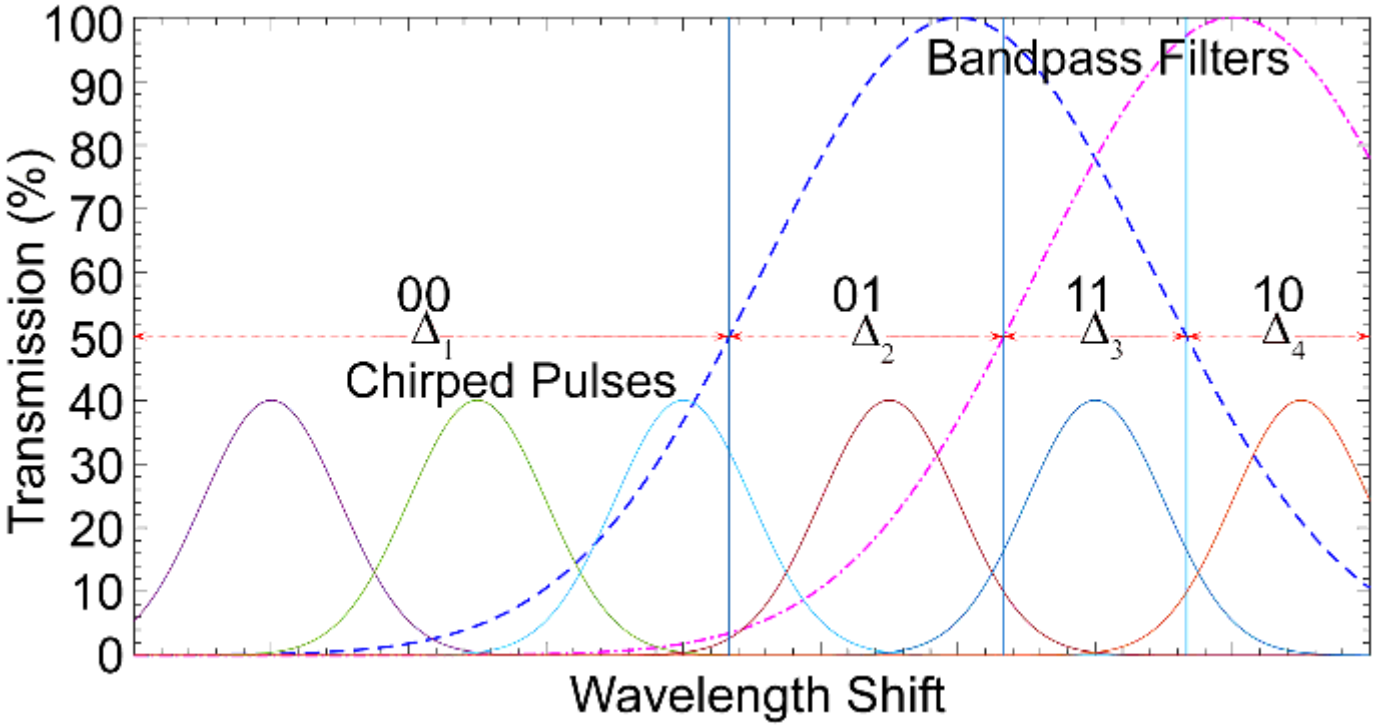

Figure 4

The two PhC-CDFs transmission spectra to compensate for the nonlinear relation of Δλout and Ein in PhC-SOA

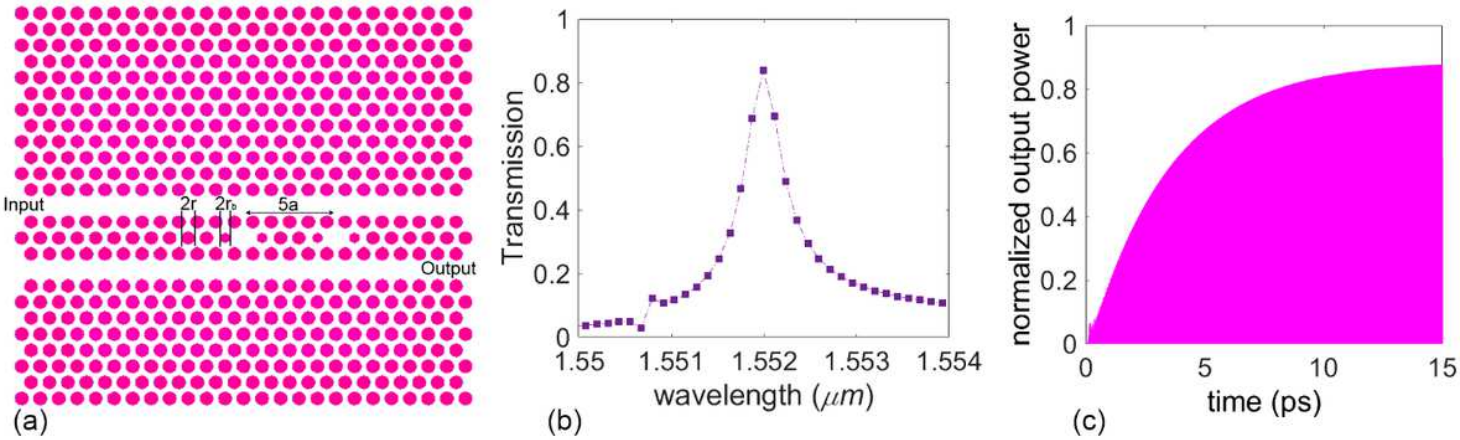

Figure 5

PhC-CDF (a) schematic, (b) transmission spectra, and (c) its time evolution at the resonance wavelength

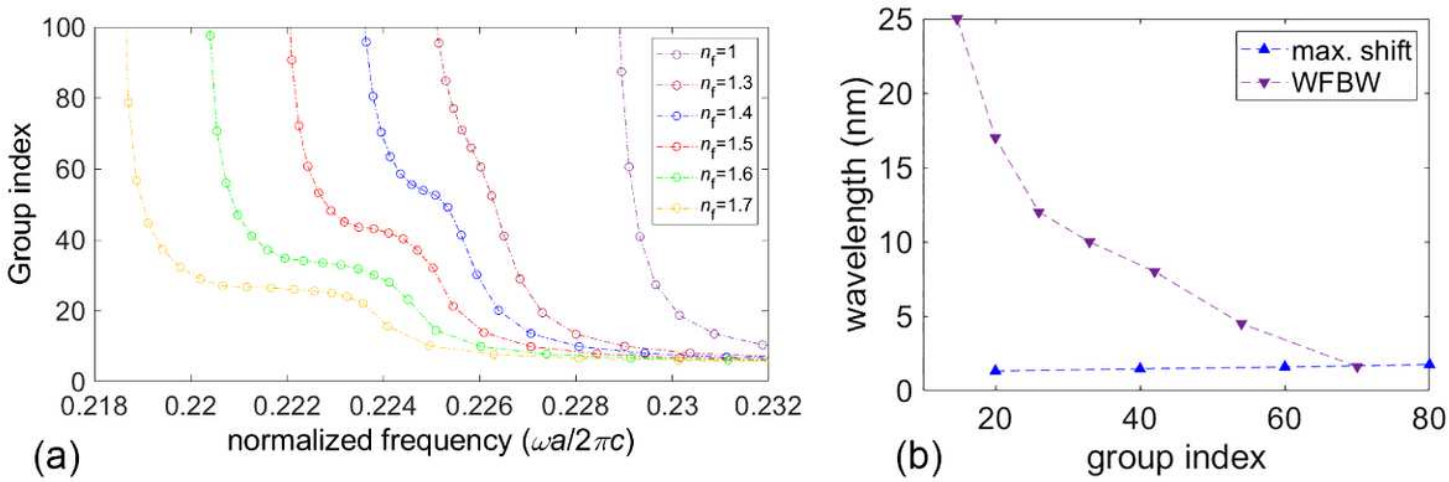

Figure 6

(a) ng versus the normalized frequency for different values of microfluidic infiltration; (b) the maximum shift required and the FBSL bandwidth for different values of ng

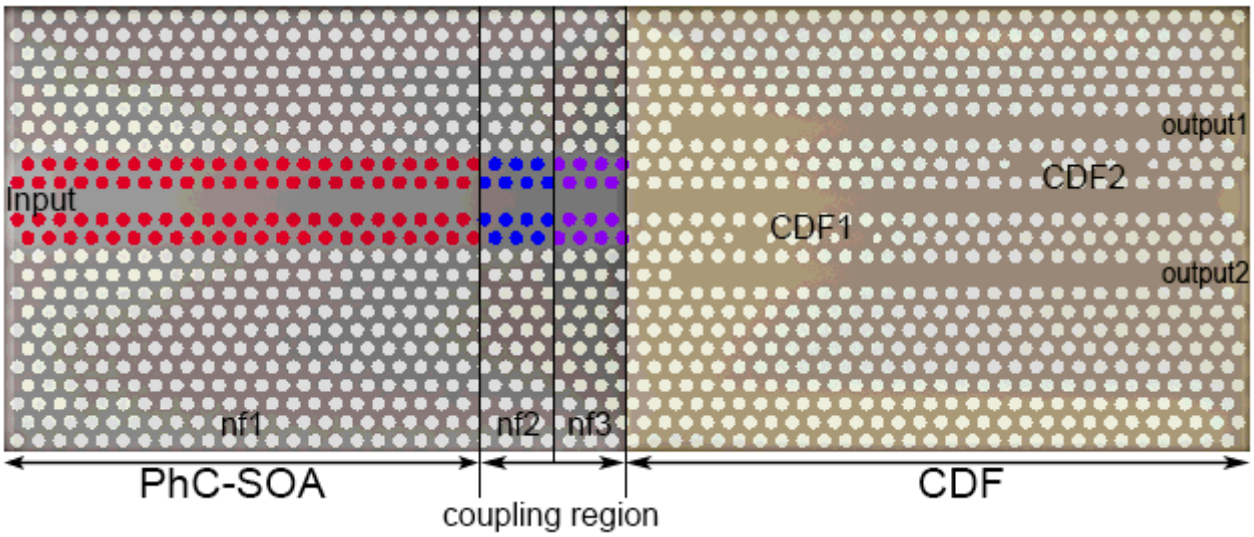

Figure 7

The proposed AO-ADC

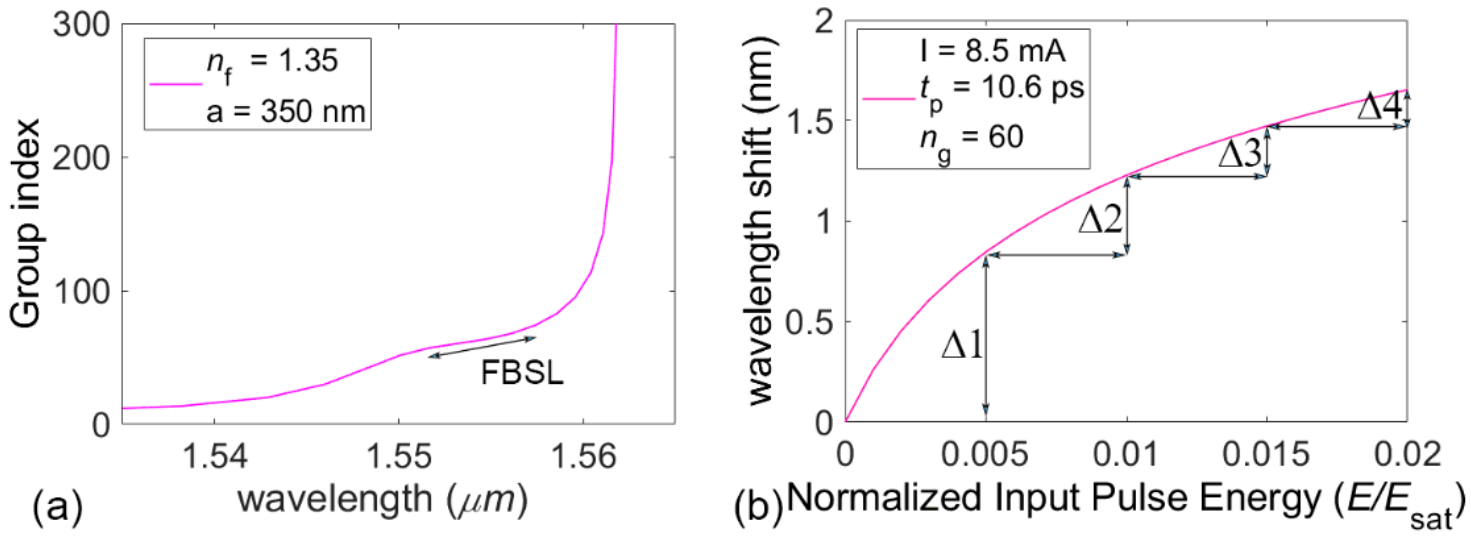

Figure 8

ng versus the wavelength for nf=1.35, and the amount of FBSL bandwidth for ng=60, (b) the amount of wavelength shift for ng=60

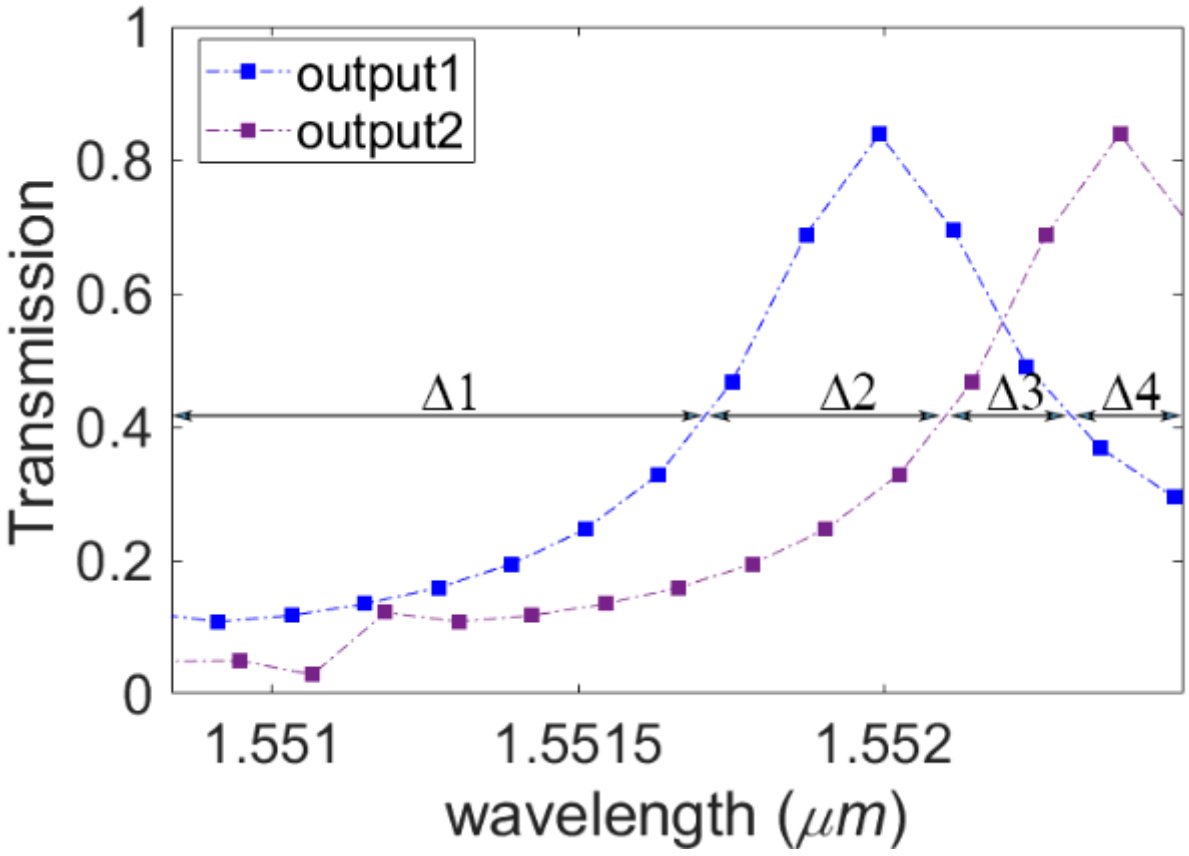

Figure 9

PhC-CDF output versus the wavelength compatible with coding the chirped signal with the characteristic shown in Fig. 8(b)

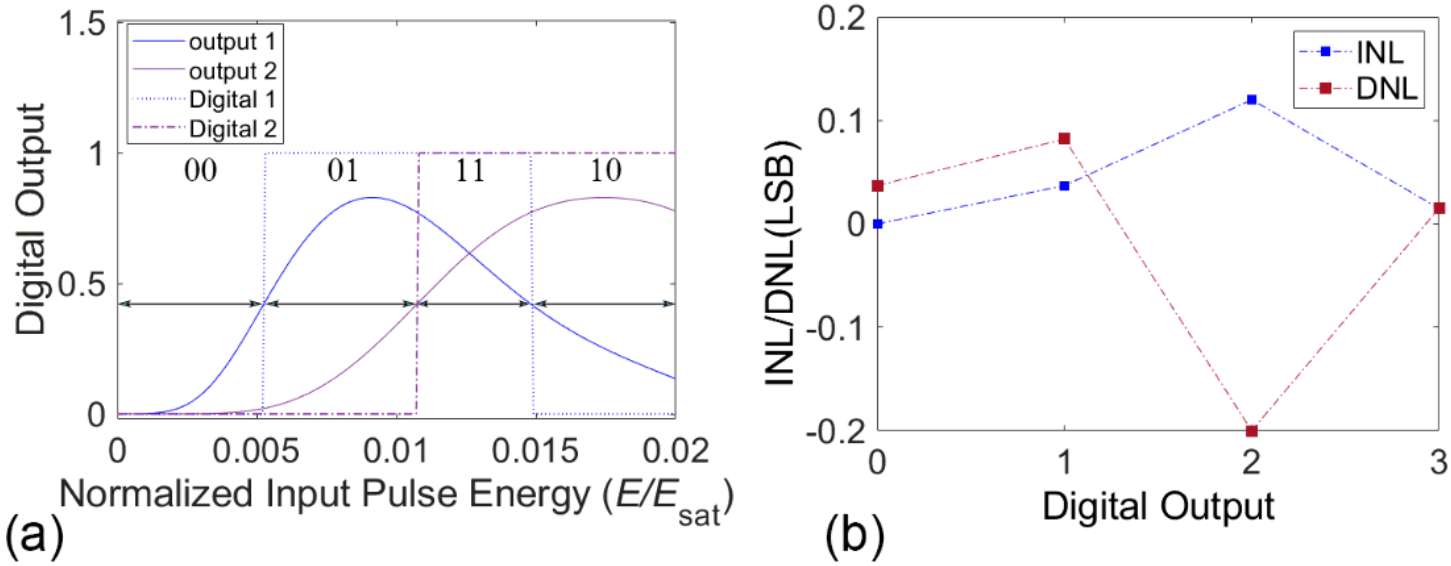

Figure 10

Normalized output power and the relative digital outputs versus the input pulse energy; (b) INL and DNL errors for each binary state